FREQUENCY DOMAIN OPTICAL TOMOGRAPHY IN HUMAN TISSUE

Yuqi Yao*, Yao Wang*, Yaling Pei*, Wenwu Zhu*, Jenhun Hu* and Randall L. Barbour+

* Polytechnic University, Brooklyn, NY 11201

+ SUNY Health Science Center, Brooklyn, NY 11203

ABSTRACT

In this paper, a reconstruction algorithm for frequency-domain optical tomography in human tissue is presented. A fast and efficient multigrid finite difference (MGFD) method is adopted as a forward solver to obtain the simulated detector responses and the required imaging operator. The solutions obtained from MGFD method for 3-D problems with weakly discontinuous coefficients and strongly discontinuous coefficients are compared with analytical solutions to determine the accuracy of the numerical method. Simultaneous reconstruction of both absorption and scattering coefficients for tissue-like media is accomplished by solving a perturbation equation using the Born approximation. This solution is obtained by a conjugate gradient descent method with Tikhonov regularization. Two examples are given to show the quality of the reconstruction results. Both involve the examination of anatomically accurate optical (AAO) models of tissue derived from segmented 3-D magnetic resonance images (MRI) to which have been assigned optical coefficients to the designated tissue types. One is a map of a female breast containing two small "added pathologies", such as tumors. The other is a map of the brain containing a "local bleeding" area, representing a hemorrhage. The reconstruction results show that the algorithm is computationally practical and can yield qualitatively correct geometry of the objects embedded in the simulated human tissue. Acceptable results are obtained even when 10% noise is present in the data.

1. INTRODUCTION

The potential for generating cross-sectional maps of tissue using NIR optical tomographic illumination schemes has stirred an intense research effort [1-5]. The numerical methods such as finite difference method [6], finite element method [7] and multigrid finite difference method [8] have been used to solve the forward and inverse problem. Recently, our group has described an efficient and practical approach for optimizing data collection and analysis strategies based on evaluation of MR-derived priors [9-11]. The basic approach involves assignment of optical coefficients to segmented 3-D MRI data to generate AAO models of tissue.

In this paper we consider the reconstruction of optical properties of small objects (such as tumors, bleeding, etc) embedded in an inhomogeneous background medium (such as human tissue). A finite number of source-detector pairs of known locations is used to probe the entire medium. Our goal is to retrieve both geometry and optical parameters (inverse problem) of objects by measuring their effects on the propagation of near-infrared light. The nonlinear inverse scattering problem is linearized within the Born approximation for this study. A fast and efficient numerical method, a multigrid finite difference (MGFD) method [12-14], is also ultilized to calculate the scattered field at detector points, which is defined as the difference between the total field with and without the added objects, and the required imaging operator which depends on the Green's function and the incident field (the latter would be the total field in Born iterative algorithm [15]). As is demonstrated, the method is well suited for accurately computing the expected field even in the presence of strong discontinuities.

The accuracy of MGFD method is verified by comparison with analytical solutions. Simultaneous reconstruction of both absorption and scattering coefficients are accomplished by employing a conjugate gradient descent (CGD) method with Tikhonov regularization. Two common problems encountered in

0-8194-1929-X/95/$6.00

medical diagnosis are studied. One of them refers to the female breast cancer and another one relates to hemorrhage. In our study, the optical properties of normal female breast and human brain are derived from segmented 3-D magnetic resonance images. Two small "added pathologies" simulating tumors, are embedded in the simulated breast. Local bleeding in the ventricle are simulated in the brain. The sources and detectors are distributed on a circle around the breast and the brain. The reconstructed results show that the algorithm can efficiently determine the geometry of the objects embedded in tissue-like media and perform well even when 10% noise is present. However we also observe that quantitative values of optical properties of the objects are not reconstructed accurately. This is due to the application of Born approximation. Born iterative scheme described in an accompanying paper [15] is expected to yield more accurate result.

2. FORWARD CALCULATION USING A MULTIGRID METHOD

The frequency domain diffusion equation for the fluence rate $u(\mathbf{r})$ is:

$$\nabla \cdot [D(\mathbf{r})\nabla u(\mathbf{r})] + [-\mu_a(\mathbf{r}) + i\frac{\omega}{v}]u(\mathbf{r}) = -S(\mathbf{r}), \quad \mathbf{r} \in \Omega \tag{1}$$

where

$$u(\mathbf{r}) \text{ and } n(\mathbf{r}) \cdot (D(\mathbf{r})\nabla u(\mathbf{r})) \text{ are continuous at } \mathbf{r} = (x, y, z) \text{ for almost every } \mathbf{r} \in \Gamma \tag{2}$$

Here Ω is a bounded region within the tissue, Γ is the internal boundary of Ω, $n(\mathbf{r})$ is the normal vector of Γ, v is the speed of light in the tissue, and S($\mathbf{r}$) represents source terms. $D(\mathbf{r}) = [3(\mu_a(\mathbf{r}) + \mu_s'(\mathbf{r}))]^{-1}$ is the diffusion coefficient, and $\mu_a(\mathbf{r})$ and $\mu_s'(\mathbf{r})$ are the absorption and equivalent-isotropic scattering coefficients, respectively. Most generally these quantities are position-dependent.

For human tissues, strong discontinuities in $\mu_a(\mathbf{r})$ and $\mu_s'(\mathbf{r})$ (or$D(\mathbf{r})$) exist. For example, there are many anatomical regions in the human body where migrating photons could encounter optically clear or free space regions. Examples include the pleural cavity, joint spaces, fluid-filled cysts, and cerebro-spinal fluid. The multigrid method is proven to be very efficient at solving the 3-D diffusion equation even with strong discontinuities in the diffusion coefficient [12].

2.1 The Multigrid Finite Difference Method

To solve Eq. (1), the finite different method partitions the domain Ω into small volume elements (voxels) and approximates the differential operator by difference, this yields:

$$\begin{aligned}
&\frac{D_{i+1/2,j,k}}{\Delta x^2}(u_{i+1,j,k} - u_{i,j,k}) - \frac{D_{i-1/2,j,k}}{\Delta x^2}(u_{i,j,k} - u_{i-1,j,k}) \\
+&\frac{D_{i,j+1/2,k}}{\Delta y^2}(u_{i,j+1,k} - u_{i,j,k}) - \frac{D_{i,j-1/2,k}}{\Delta y^2}(u_{i,j,k} - u_{i,j-1,k}) \\
+&\frac{D_{i,j,k+1/2}}{\Delta z^2}(u_{i,j,k+1} - u_{i,j,k}) - \frac{D_{i,j,k-1/2}}{\Delta z^2}(u_{i,j,k} - u_{i,j,k-1}) \\
&+(-\mu_{a_{i,j,k}} + i\frac{\omega}{v})u_{i,j,k} = S_{i,j,k},
\end{aligned} \tag{3}$$

where i, j and k are the voxel indices for axes x, y and z, respectively, $\Delta x, \Delta y$ and Δz are the mesh size in x, y and z directions, respectively, and $D_{i,j,k} = D(i\Delta x, j\Delta y, k\Delta z)$.

Eq. (3) can also be denoted by:

$$Lu = f, \tag{4}$$

where the operator L depends on the medium properties $D_{i,j,k}$, and f depends on the source distribution. Rather than solving $u_{i,j,k}$ at a fine grid directly, the multigrid method solves u from a coarse grid to the

fine grid progressively. Among several multigrid schemes we use the full multigrid (FMG) method [14]. Letting the number of grid levels be denoted by M, we represent the original equation in (4) on the finest grid by

$$L^M u^M = f^M. \tag{5}$$

The operator on the coarse grid is defined recursively as:

$$L^{k-1} = (I^k{}_{k-1})^T L^k I^k{}_{k-1}, \tag{6}$$

where $I^k{}_{k-1}$ is the coarse-to-fine operator from grid $k-1$ to k using multilinear interpolation. The source term on the $(k-1)$th grid is given by:

$$f^{k-1} = (I^k{}_{k-1})^T r^k, \tag{7}$$

where

$$r^k = f^k - L^k \tilde{u}^k, \tag{8}$$

is the residual on grid k. Finally, we use a relaxation sweep process given by the expression

$$u^k \longleftarrow G^k(\tilde{u}^k, f^k) \tag{9}$$

where G^k represents the sweeps of some iterative process, such as the point Gauss-Seidel relaxation, line Gauss-Seidel (in any combination of directions) relaxation and planar Gauss-Seidel (for three-dimensional problems) relaxation.

Fig. 1 illustrates the basic idea of the FMG algorithm for a problem with $M = 4$ grid levels. The process starts on the coarsest grid $l = 1$ where the discrete approximation to Eq. (3) on this grid level is solved. The resulting solution is interpolated to the next finer grid $l = 2$ and used as the first approximation to

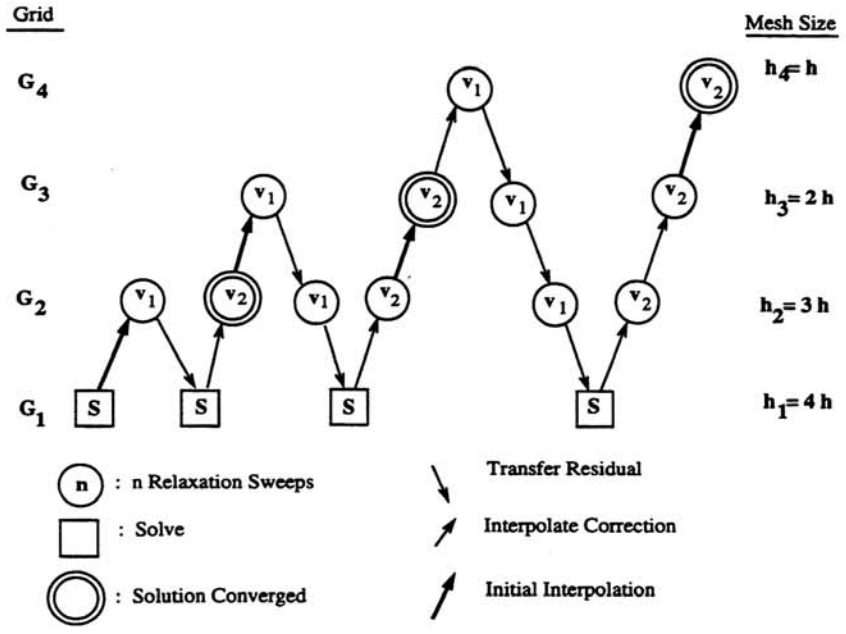

Figure 1: A Full Multigrid (FMG) algorithm for a problem with $M = 4$ grids (from [14]).

the solution of this grid level. The residual is then solved by a multigrid V-cycle. This process is repeated, interpolating the solution from one level to the next as a first approximation and solving the residual by a

V-cycle, until the final solution is obtained on the finest level $l = M$. In going from one level l to the next finer level, $l+1$, the truncation error (discrete approximation of the actual continuous function) decreases by roughly the mesh element size ratio $(h_{l+1}/h_l)^p$, where h_l is the side length of an element at grid level l, and p is the order of the difference approximation. The solution at each grid level by the FMG algorithm (denoted by the double circles in Fig. 1) is accurate to at least the level of the respective truncation error. Therefore, the FMG algorithm is very efficient.

2.2 Results of Forward Calculations

To evaluate the accuracy of the MGFD algorithm, we compare its solution to one obtained using an analytical solver [2] for a simple medium. We consider a spherical object embedded in an otherwise homogeneous infinite medium. To simulate the solution using the MGFD, we make the following assumptions:

(1) A spherical object with a radius of 0.7 cm is embedded in a cube of volume 1000 cm^3. The problem is to determine the incident field and scattered field over a ring of radius 4 cm surrounding the object.

(2) To simulate a weak discontinuity, the optical properties of the background and object are $\mu_a^b = 0.05cm^{-1}$, $\mu_s'^b = 10.0cm^{-1}$ and $\mu_a = 0.1cm^{-1}$, $\mu_s' = 20.0cm^{-1}$, respectively. We use the Dirichlet condition $u = 0$ on the boundary.

(3) To simulate a strong discontinuity, the optical properties of the background and object are $\mu_a^b = 0.01cm^{-1}$, $\mu_s'^b = 0.5cm^{-1}$, and $\mu_a = 1.0cm^{-1}$, $\mu_s' = 30.0cm^{-1}$, respectively. This represents a 100 fold difference in the absorption coefficient and a 60 fold difference in the scattering coefficient. We require that u, the total field, be equal to the incident field on the boundary.

Fig. 2 shows the comparison of the amplitude and phase of the incident field and scattered field obtained

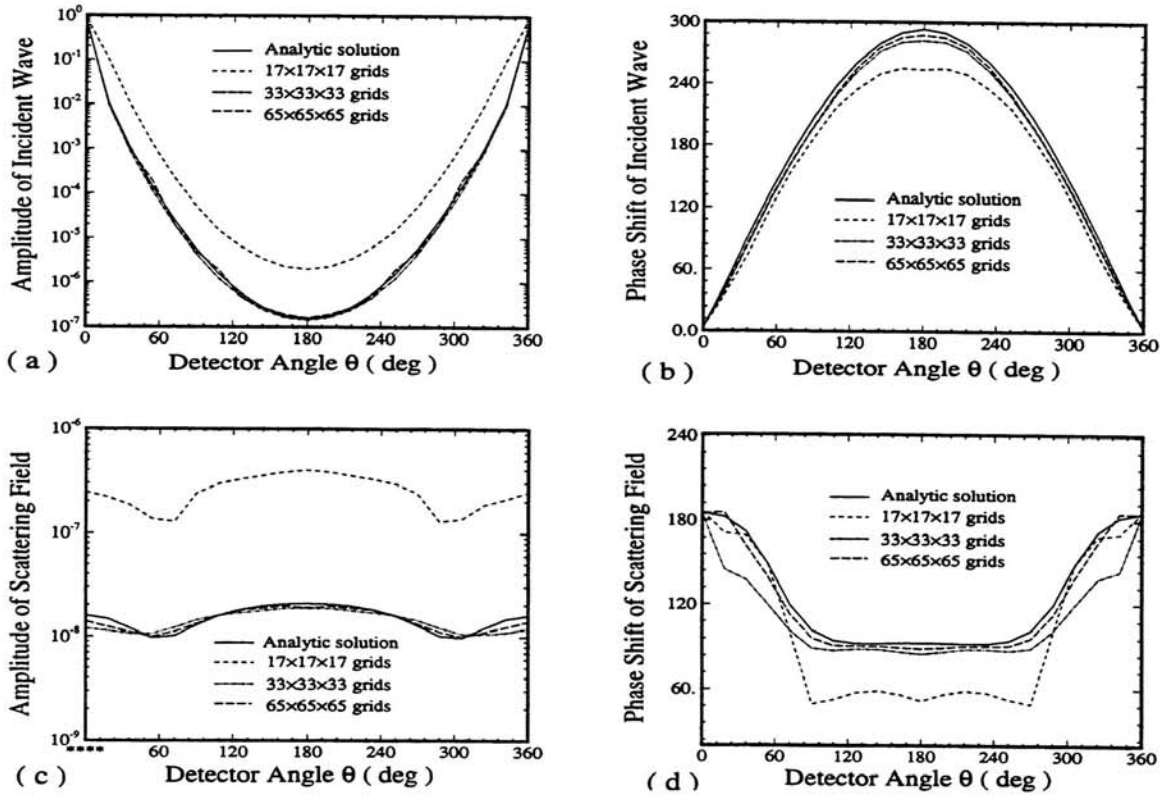

Figure 2: Amplitude and phase of the incident and scattered field versus detector angle for different grid spacing, due to a 0.7 cm radius object with $\mu_a = 0.1cm^{-1}$ and $\mu'_s = 20.0cm^{-1}$ embedded in surrounding background media with $\mu_a^b = 0.05cm^{-1}$ and $\mu_s'^b = 10.0cm^{-1}$. The modulation frequency is 200MHz.

by the analytical solution and MGFD method for the weak perturbation problem. For the MGFD method, we show the results obtained when the $1000cm^3$ cube is discretized into different numbers of mesh elements. We clearly see that the MGFD algorithm results with $33\times33\times33$ ($h \simeq 3mm$) and $65\times65\times65$ ($h \simeq 1.5mm$) elements are very close to the analytic solution. On the other hand, the results obtained with a $17\times17\times17$ ($h \simeq 6mm$) elements deviate significantly (a factor of 10 in the amplitude data) from the analytic solution.

Results in Fig. 3 show the comparison of the analytic and MGFD solutions for the strong perturbation problem. In this case, it can be seen that for amplitude data, reasonably accurate results are obtained for the incident field for $33 \times 33 \times 33$ and $65 \times 65 \times 65$ grid sizes, at least for larger detector angles. Results shown in the phase plots illustrate that comparable results are obtained for the two grid sizes using the MGFD method, but differ from the analytic result by approximately a 15 degree positive off-set.

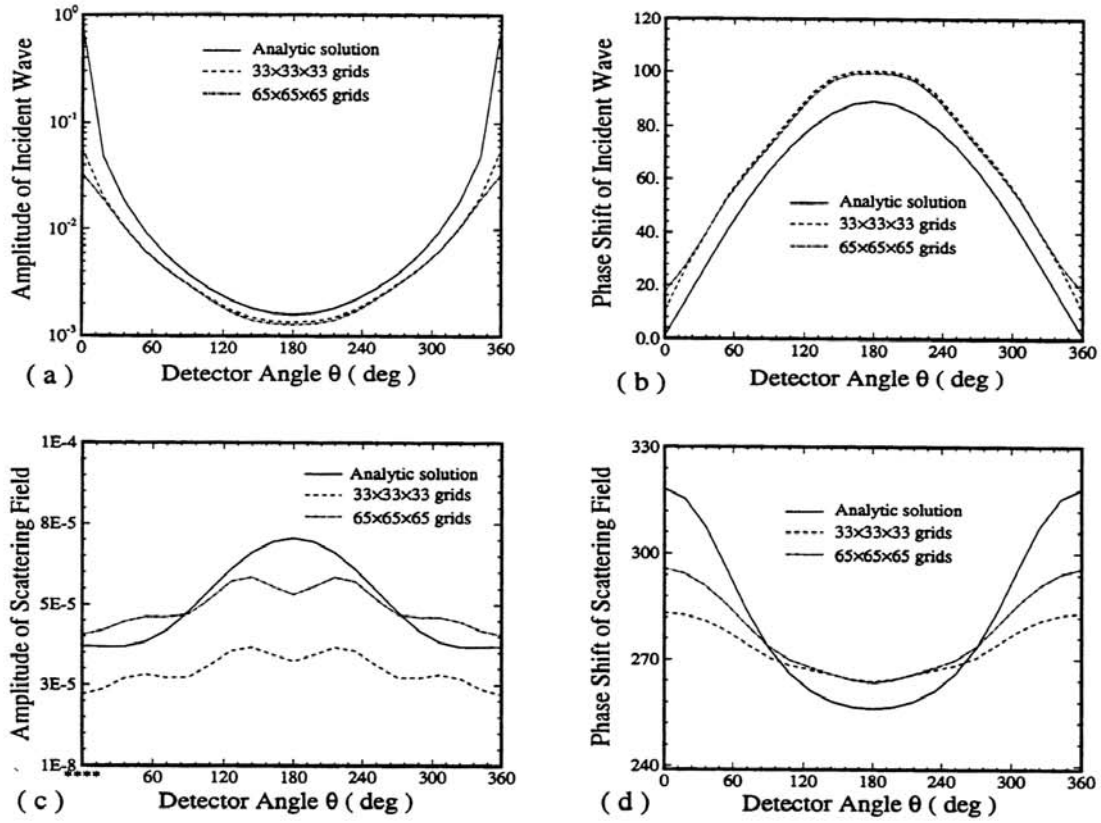

Figure 3: Amplitude and phase of the incident and scattered field versus detector angle for different grid spacing, due to a 0.7 cm radius object with $\mu_a = 1.0cm^{-1}$ and $\mu'_s = 30.0cm^{-1}$ embedded in surrounding background media with $\mu_a^b = 0.01cm^{-1}$ and $\mu_s^{'b} = 0.5cm^{-1}$. The modulation frequency is 200MHz.

Interestingly, somewhat more accurate results are obtained for the computed amplitude of the scattered field, particular for the larger grid size. The phase data also show improved agreement with the analytic result using the larger grid size.

3. IMAGE RECONSTRUCTION FORMULATION

3.1 The Mathematical Model

Consider an unknown 3-D object $O(\mathbf{r})$ (*e.g.*, tumor) occupying volume V_{oj} in some inhomogeneous background (human tissue) space. The receivers collect the signal of the field scattered by the object due to each of the transmitted field. The goal is to simultaneously reconstruct the absorption and scattering distributions of the scatterer as a function of the three space variables x, y and z.

From Eq. (1), we can derive the inhomogeneous scalar wave equation for photon density waves:

$$\nabla^2 u(\mathbf{r}) + k_b^2(\mathbf{r})u(\mathbf{r}) = S(\mathbf{r}) - \mathcal{L}(\mathbf{r})u(\mathbf{r}), \tag{10}$$

where ${k_b}^2(\mathbf{r}) = -\mu_a^b(\mathbf{r})/D_b(\mathbf{r}) + i\omega/vD_b(\mathbf{r})$ is the wavenumber of the inhomogeneous background medium, the object operator $\mathcal{L}(\mathbf{r})$ is

$$\mathcal{L}(\mathbf{r}) = O(\mathbf{r}) + \frac{\nabla D(\mathbf{r}) \cdot \nabla}{D(\mathbf{r})}, \quad r \epsilon V_o \tag{11}$$

The object function $O(\mathbf{r})$ is:

$$O(\mathbf{r}) = k^2(\mathbf{r}) - {k_b}^2(\mathbf{r}), \tag{12}$$

where $k^2(\mathbf{r}) = -\mu_a(\mathbf{r})/D(\mathbf{r}) + i\omega/vD(\mathbf{r})$. From Eq. (10), it can easily be shown that the scattering field satisfies the following nonlinear volume intergral equation:

$$u_s(\mathbf{r}) = \int_v G(\mathbf{r}, \mathbf{r}')\mathcal{L}(\mathbf{r}')u(\mathbf{r}')d^3\mathbf{r}', \tag{13}$$

where

$$u_s(\mathbf{r}) = u(\mathbf{r}) - u_b(\mathbf{r}) \tag{14}$$

is the scattered field measured at the detector, $u(\mathbf{r})$ is the total field inside the object due to the sources, $u_b(\mathbf{r})$ is the background field without object due to the sources, and the inhomogeneous background Green's function satisfes:

$$\nabla^2 G(\mathbf{r}, \mathbf{r}') + k_b^2(\mathbf{r})G(\mathbf{r}, \mathbf{r}') = -\delta(\mathbf{r} - \mathbf{r}') \tag{15}$$

In the cases when the contrast of the scatterer is weak so that the second term on the right of Eq. (11) is small compared to the first term, we can neglect the second term. In addition, we adopt the first-order Born approximation $u(\mathbf{r}) \cong u_b(\mathbf{r})$. Then Eq. (13) can be approximated as

$$u_s(\mathbf{r}) = \int_v G(\mathbf{r}, \mathbf{r}')O(\mathbf{r}')u_b(\mathbf{r}')d^3\mathbf{r}' \tag{16}$$

3.2 Simultaneous Reconstruction of Absorption and Scattering Distributions

The integral equation in (16) can be discretized to yield a linear system of equations with complex coefficients as follows:

$$\mathbf{W_{(m \times n)} o_{(n)}} = \mathbf{u_{(m)}} \tag{17}$$

where $\mathbf{O} = [O(\mathbf{r}_j, j = 1, 2, \cdots, n]^T$ is composed of the values of $O(\mathbf{r})$ at various voxels $\mathbf{r}_j$; $\mathbf{u} = [u_s(\mathbf{r}_{d_i}, \mathbf{r}_{s_i}), i = 1, 2, \cdots, m]^T$ consists of the scattered field obtained with different source-detector pairs $(\mathbf{r}_{d_i}, \mathbf{r}_{s_i})$; and $\mathbf{W}$ is a weight matrix with elements:

$$W_{ij} = G(\mathbf{r}_{d_i}, \mathbf{r}_j)u_b(\mathbf{r}_{s_i} - \mathbf{r}_j)\delta v, \quad i = 1, \cdots m, j = 1, \cdots n, \tag{18}$$

where δv is the volume of a voxel. The weight matrix depends on the physics of the problem (such as the properties of the background medium, the Green's function, the incident field, and measurement geometry).

It is well known that Eq. (17) of the inverse scattering problem is ill-posed. In order to find an adequate solution of Eq. (17), the Tikhonov regularization procedure [16-17] is employed to circumvent the instability of the problem. In this procedure, the following function $E(\cdot)$ is minimized:

$$E(\mathbf{o}) = ||\mathbf{W} \cdot \mathbf{o} - \mathbf{u}||^2 + \gamma ||\mathbf{H} \cdot \mathbf{o}||^2, \tag{19}$$

where γ is the regularization parameter, and $\mathbf{H}$ is the smoothing matrix which is chosen to be an identity matrix in this paper. The regularized solution is given by

$$\mathbf{o} = [\mathbf{W}^+ \cdot \mathbf{W} + \gamma \mathbf{H}^+ \cdot \mathbf{H}]^{-1} \cdot \mathbf{W}^+ \cdot \mathbf{u} \tag{20}$$

where $\mathbf{W}^+$ and $\mathbf{H}^+$ are the conjugate transpose of $\mathbf{W}$ and $\mathbf{H}$, respectively. This solution is obtained by the conjugat gradient descent method.

Once the object function is obtained, we can determine the absorption and scattering coefficients as follows [15]:

$$\delta\mu_a(\mathbf{r}) = -\frac{\mu_a^b \frac{Im[O(\mathbf{r})]}{\omega/c} + Re[O(\mathbf{r})]}{\frac{Im[O(\mathbf{r})]}{\omega/c} + 3(\mu_a^b + \mu_s'^b)} \tag{21}$$

and

$$\delta\mu_s'(\mathbf{r}) = \frac{\{Re[O(\mathbf{r})] + 3(3\mu_a^b + \mu_s'^b) + \frac{Im[O(\mathbf{r})]}{\omega/c}\}\frac{Im[O(\mathbf{r})]}{3\omega/c}}{\frac{Im[O(\mathbf{r})]}{\omega/c} + 3(\mu_a^b + \mu_s'^b)}. \tag{22}$$

4. SIMULATION RESULTS

In this section, we show the reconstruction results on the simulated female breast containing "added pathologies" and the simulated human brain containing "added bleeding". The optical properties in these media are derived based on anatomic maps obtained from 3-D magnetic resonance images (MRI). Segmentation of the breast data was achieved using a thresholding method followed by identify and deleting isolated regions [18]. Multispectral MR images of the brain were obtained and segmented based on both spatial and spectral information [19].

4.1 Results on the Simulated Female Breast

Fig. 4(a) illustrates the configuration of sources and detectors (S/D) for the breast imaging simulation, where the S/D are uniformly spread on a ring surrounding an axial slice perpendicular to the chest wall. A total of 10 sources and 20 detectors are on the surface of the breast. To overcome zero boundary on the surface of the breast, we use a "matching medium" to surround the breast. The optical properties of the matching medium are $\mu_a = 0.4cm^{-1}$ and $\mu_s' = 10.0cm^{-1}$ which are the same as those of fat. At the "matching medium" boundary, the Dirichlet condition $u = 0$ is applied. The "matching medium" has two physical significances: (1) Enhanced sensitivity to embedded objects for image reconstruction is achieved if the optical properties of this medium are appropriately chosen [3]; (2) To serve as a possible mechanical support for sources and detectors located on the surface of tissue.

The breast has a volume of $9 \times 8 \times 7cm^3$, and the total volume being solved (with the matching medium surrounding the breast) is $10 \times 10 \times 10cm^3$. The breast was segmented into two different tissue types: fat and parenchyma. Each tissue type was assigned a set of optical properties of absorption coefficient μ_a and reduced scattering coefficient μ_s', respectively. Two spherical "pathologies" were introduced by assigning different μ_a and μ_s' values to selected voxels in two regions. Fig. 4(b) shows the anatomic map of a sagittal slice perpendicular to the chest wall. Fig. 4(c) shows the image of absorption coefficients in an axial slice in the background medium. The optical properties for different tissues are listed in Table 1.

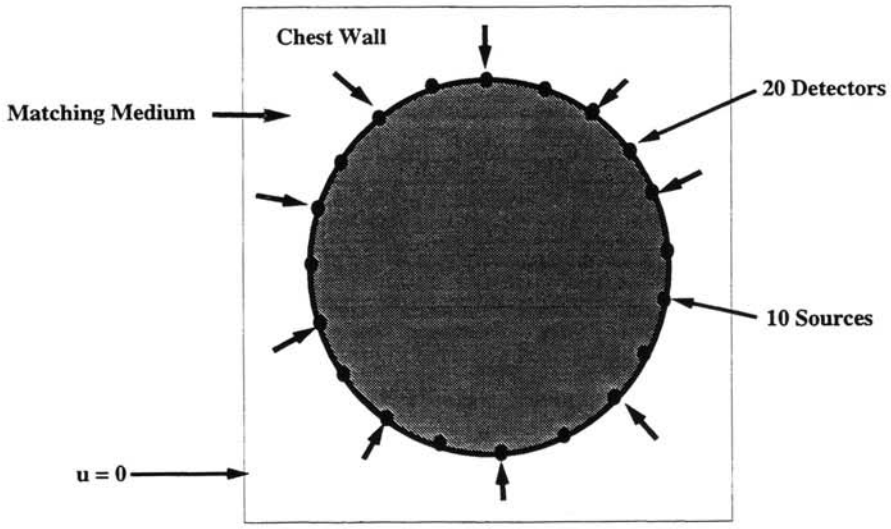

(a)

(b)

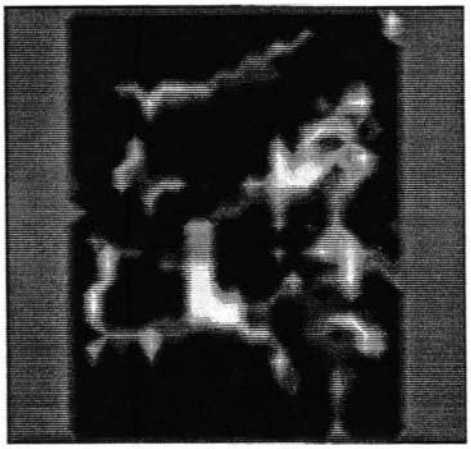

(c)

Figure 4: (a) Illustration of position of source-detector configuration used. (b) Segmentation of the tenth sagittal cut of MR breast images. The black color represents fat tissue, the white cooar represents parenchyma tissue. (c) Image of the absorption properties of an axial slice.

Table 1: Optical Properties Assigned to Different Tissue Types in the Simulated Female Breast (Unit: cm^{-1})

Fat		Parenchyma		Tumor 1		Tumor 2	
μ_a	μ_s'	μ_a	μ_s'	$\delta\mu_a$	$\delta\mu_s'$	$\delta\mu_a$	$\delta\mu_s'$
0.04	10.0	0.08	7.0	0.1	10.0	0.16	15.0

The two objects each has a radius of 0.7 cm, separated by 3 cm. The optical properties of the two objects are different as listed in Table 1. The forward data was calculated on a $65 \times 65 \times 65$ grid in full volume ($1000cm^3$). However to reduce computation, the reconstruction was performed only for a single axial slice with 65×65 grid. The weights for this 2-D slice are obtained by adding the weights in all the axial slices. This is equivalent to assume that all the voxels in the same axial positions have the same optical properties. The reconstruction image is an approximation to the average of all axial slices. In order to evaluate the effect of noise in the data on the reconstruction accuracy, we compare results from the original calculated data and those subjected to 10% (SNR=20 dB) noise. Fig. 5(a) is the actual distribution of the magnitude of the object function (see Eq. (12)). Figs. 5(b) and 5(c) are the reconstructed object functions (magnitude only) from the original and noise added data, respectively. Figs. 5(d)-5(f) present similar results for the perturbation in absorption, while Figs. 5(g)-(i) are for the perturbation in scattering. It can be seen that with this example, the reconstruction results are only accurate qualitatively, correctly identifying the presence of two objects. But the estimated spatial range and perturbation magnitude of the object are not very accurate. With noise-free data, the two rods are located quite accurately with slight blurring, and the estimated perturbation magnitude is approximately half of the actual one. But with noise-added data, the objects are poorly located (especially for the scattering properties) and the peak perturbation values are severely underestimated.

4.2 Results on the Simulated Human Brain

For the brain imaging simulation, the S/D are evenly spread over a mid axial slice. Fig 6(a) shows the anatomic map of this slice. The brain was segmented into four different tissue types: CSF, bone, gray matter and white matter. Each tissue type was assigned a set of optical properties of μ_a and μ_s'. A "bleeding" is introduced in the ventricle area by assigning different μ_a and μ_s' values to selected voxels. Fig. 6(b) shows the inhomogeneous background medium (absorption coefficient) on the detector cross section. Fig. 6(c) shows the position of the "added bleeding" with $\delta\mu_a = 1.0cm^{-1}$ and $\delta\mu_s' = 6.0cm^{-1}$. The optical properties assigned to different tissue types are listed in Table 2. The sources and detectors are embedded in a "matching medium" outside the brain. The optical properties of this medium are the same as those of the CSF.

The forward calculation was done in 3-D, with $65 \times 65 \times 65$ grid size in a volume of $8.5 \times 8 \times 9cm^3$. The reconstruction was only performed for the axial slice shown in Fig. 6(b). As with the breast simulation, the weight for this slice was obtained by adding the weights in all the axial slices. The reconstructed object function (magnitude) is shown in Fig. 6(d). The results are obtained by the CGD algorithm after 5000 iterations in the absence of added noise. The modulation frequency is 200 MHz.

Table 2: Optical Properties Assigned to Different Tissue Types in the Simulated Human Brain (Unit: cm^{-1})

CSF		Bone		Gray matter		White matter		Bleeding	
μ_a	μ_s'	μ_a	μ_s'	μ_a	μ_s'	μ_a	μ_s'	$\delta\mu_a$	$\delta\mu_s'$
0.01	0.5	0.01	5.0	0.2	10.0	0.1	15.0	1.0	6.0

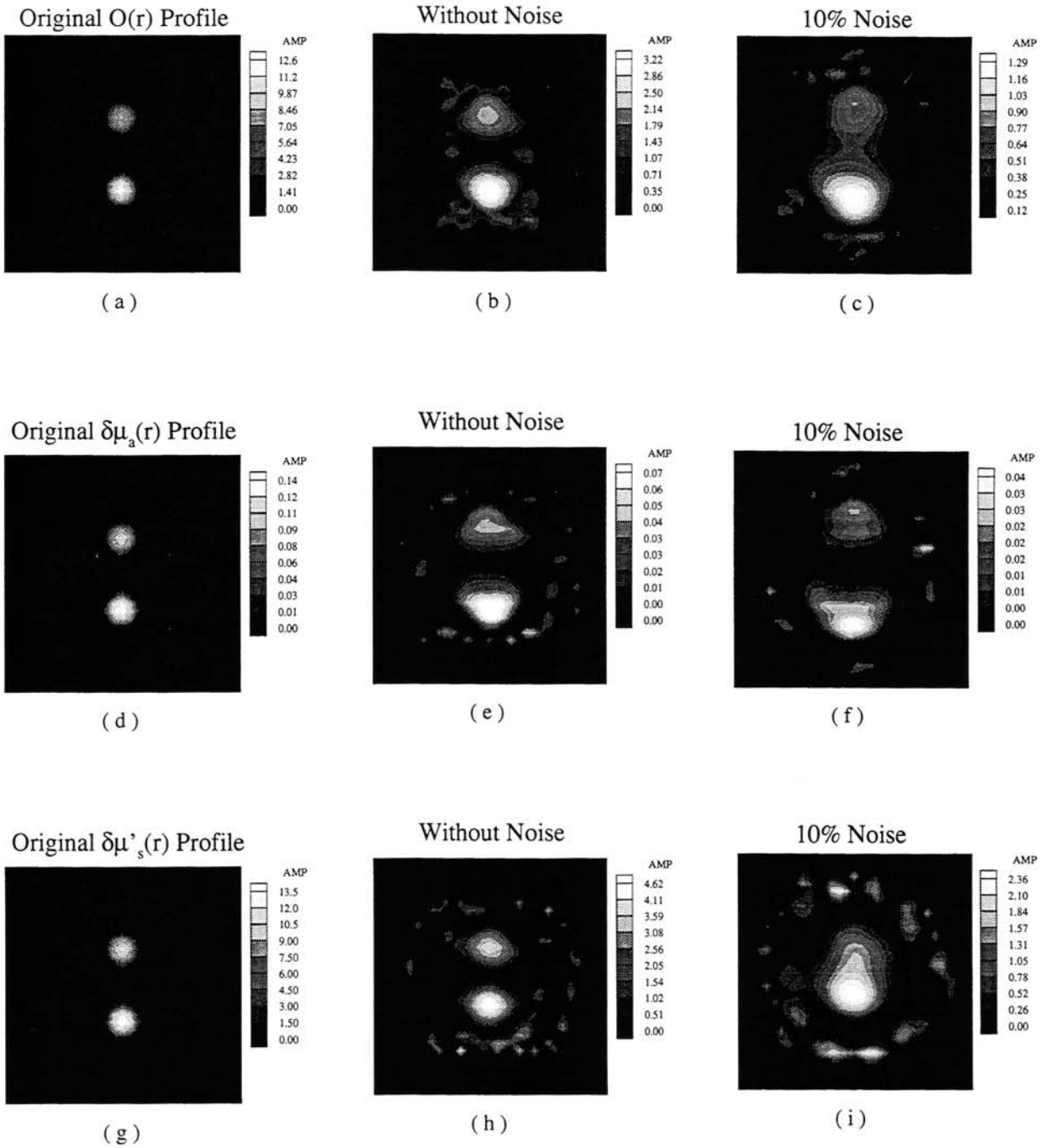

Figure 5: Simultaneous reconstruction of the object function, the absorption and scattering distributions of two sin-like objects with same radius (0.7 cm) and different optical properties (see Table 1). The two objects separated by 3 cm are embedded in an axial slice of the breast with optical properties shown in Fig. 4(c). The modulation frequency is 200 MHz.

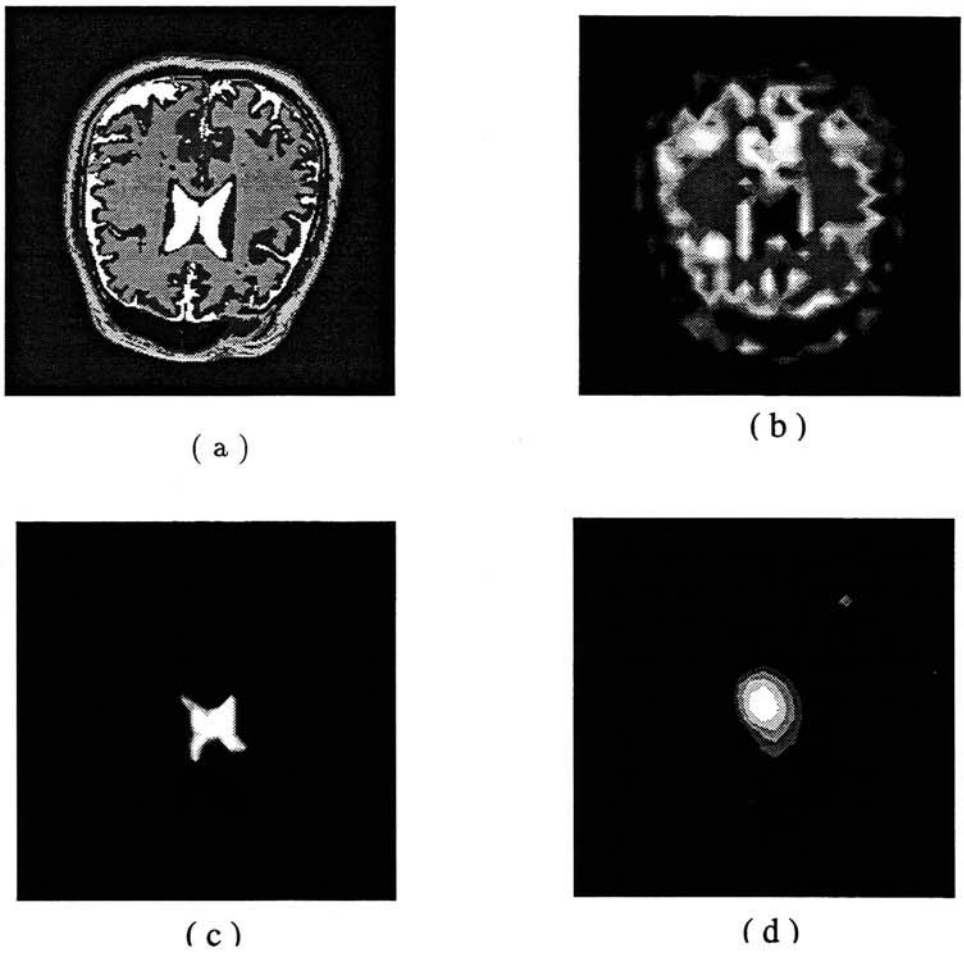

Figure 6: (a) Segmentation of the fourteenth axial cut of MR brain images. (b) Image of the absorption properties of this axial slice. (c) Illustration of position of "added bleeding" with $\delta\mu_a = 1.0cm^{-1}$ and $\delta\mu_s' = 6.0cm^{-1}$. (d) Reconstructed image of of this axial slice with added bleeding. Results shown were obtained after 5000 iterations in the absence of added noise. The modulation frequency is 200 MHz.